18th International Conference
ENGINEERING MECHANICS 2012
Svratka, Czech Republic, May 14 – 17, 2012

pp. 1505–1516
Paper #38

NON-NEWTONIAN EFFECTS OF PULSATILE BLOOD FLOW IN A REALISTIC BYPASS GRAFT GEOMETRY

J. Vimmr [*], A. Jonášová [**] O. Bublík [***]

Abstract: *The study is focused on mathematical modelling of pulsatile blood flow in a patient-specific aorto-coronary bypass model with individual graft. Blood is considered to be an incompressible non-Newtonian fluid, whose behaviour is described by the macroscopic Carreau-Yasuda model. The numerical solution of the non-linear system of incompressible Navier-Stokes equations is based on the three-stage fractional step method and the cell-centred finite volume method formulated for hybrid unstructured tetrahedral grids. Since patency and long-term performance of all implanted bypass grafts is closely related to hemodynamics, all obtained results are analysed and discussed with the help of several significant hemodynamical wall parameters such as cycle-averaged wall shear stress and oscillatory shear index.*

Keywords: ***aorto-coronary bypass, non-Newtonian fluid, fractional step method, finite volume method.***

1. Introduction

Nowadays it is generally accepted that the performance and patency of implanted bypass grafts is significantly affected by local hemodynamics, Loth et al. (2008). Beside thrombogenesis, usually originating in low flow rates or technical mistakes, Vural et al. (2001), the majority of recorded bypass failures is often caused by intimal hyperplasia, Haruguchi and Teraoka (2003). This type of intimal thickening represents a form of abnormal healing process observed at the distal anastomosis of the implanted graft, Fig. 1. The morphological and metabolic changes observed in vessel walls are hypothesised to be triggered by disturbed blood flow and low and oscillating shear stress, Bassiouny et al. (1992). In this regard, the investigation of hemodynamics in the form of numerical simulations represents a valuable contribution to the understanding of graft disease formation.

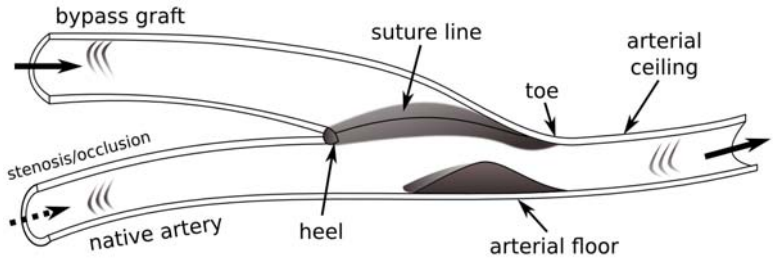

Fig. 1: Localisation of intimal thickening at the distal end-to-side anastomosis with relevant terminology, modified from Bassiouny et al. (1992).

In relation to previous modelling of steady non-Newtonian blood flow performed in an idealized complete bypass model with two end-to-side anastomoses, Vimmr and Jonášová (2010), present study tries to contribute to this investigation by modelling pulsatile non-Newtonian blood flow in a realistic aorto-coronary bypass model. The analysis and discussion of obtained numerical results is carried out with the help of two hemodynamically significant wall parameters – cycle-averaged wall shear stress (WSS) and oscillatory shear index (OSI).

[*]Doc. Ing. Jan Vimmr, Ph.D.: Department of Mechanics, University of West Bohemia, Univerzitní 22; 306 14, Pilsen; CZ, e-mail: jvimmr@kme.zcu.cz
[**]Ing. Alena Jonášová: Department of Mechanics, University of West Bohemia, Univerzitní 22; 306 14, Pilsen; CZ, e-mail: jonasova@kme.zcu.cz
[***]Ing. Ondřej Bublík: Department of Mechanics, University of West Bohemia, Univerzitní 22; 306 14, Pilsen; CZ, e-mail: obublik@kme.zcu.cz

2. Problem formulation

The main objective of this study is the analysis of hemodynamics in an individual aorto-coronary bypass graft. In cardiovascular surgery, the term individual denotes a vascular graft with one distal end-to-side anastomosis, i.e., the graft provides a direct connection between the aorta and the stenosed or occluded coronary artery. The bypass model considered in this study is reconstructed from CT data provided by the courtesy of the University Hospital in Pilsen, Czech Republic. The reconstruction process and computational mesh generation are carried out in software packages Amira and Altair Hypermesh, respectively. An example of primary reconstruction of the chest region and of the individual bypass graft is shown in Fig. 2. The final shape of the bypass model after smoothing is displayed in Fig. 3. The unstructured computational mesh used for all numerical simulations consists of 362,437 tetrahedral cells.

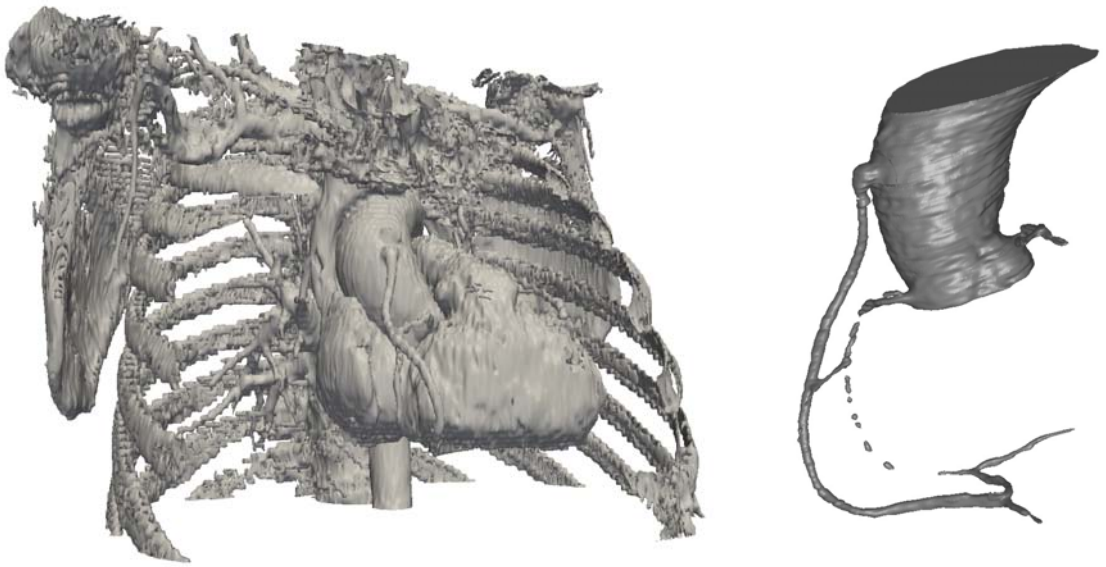

Fig. 2: CT reconstruction of the chest region (left) and of the aorto-coronary bypass graft (right)

For the purpose of blood flow simulations in the prepared individual graft, we choose an approach similar to that found in other studies published to the theme of bypass hemodynamics, see the review paper Loth et al. (2008). Firstly, taking into account the fact that at the end of the arterialisation process, venous grafts lose their compliance, all the bypass walls are, in this study, modelled as impermeable and rigid, including the wall of the aorta. In the light of this simplification, we are aware that the neglected aortic elasticity represents a considerable limitation of the present study. We hope to rectify it in one of our future projects by solving the fluid-structure interaction problem. In this study, we further assume a static aorto-coronary bypass model, i.e., the impact of heart beating is not considered. This assumption is based on the findings published in Zeng et al. (2003), where it was shown that the arterial motion does not significantly affect blood flow in the case of flow pulsatility. In order to model blood's complex rheological properties, we introduce the macroscopic non-Newtonian Carreau-Yasuda model, which we have successfully applied in our previous simulations, Vimmr and Jonášová (2010),

$$\eta(\dot{\gamma}) = \eta_\infty + (\eta_0 - \eta_\infty)\Big[1 + \big(\lambda\dot{\gamma}\big)^a\Big]^{\frac{n-1}{a}}, \tag{1}$$

where η_0 and η_∞ are the zero and infinite shear viscosities, respectively, λ is the characteristic relaxation time and n is the flow index. The five parameters occurring in the Carreau-Yasuda model (1) may be determined by numerical fitting of experimental data. In this study, we adopt data mentioned in Cho and Kensey (1991): $\eta_\infty = 3.45 \cdot 10^{-3}\,\mathrm{Pa}\cdot\mathrm{s}$, $\eta_0 = 56 \cdot 10^{-3}\,\mathrm{Pa}\cdot\mathrm{s}$, $\lambda = 1.902\,\mathrm{s}$, $a = 1.25$, $n = 0.22$. The shear rate is given as $\dot{\gamma} = 2\sqrt{D_{II}}$, where D_{II} denotes the second invariant of the rate of deformation tensor $\mathbf{D} = \frac{1}{2}\left(\nabla\boldsymbol{v} + (\nabla\boldsymbol{v})^T\right)$. For the incompressible fluid, the second invariant is defined as $D_{II} = \frac{1}{2}\,d_{ij}d_{ij}$, $i,j = 1,2,3$, where d_{ij} are the components of the rate of deformation tensor $\mathbf{D}$. For the Newtonian flow, the molecular viscosity is kept constant and equal to infinite shear viscosity η_∞. Finally, note that the coronary arteries shown in Fig. 3 are considered to be occluded (with no inflow) so that the only relevant incoming flow will be that of the bypass graft.

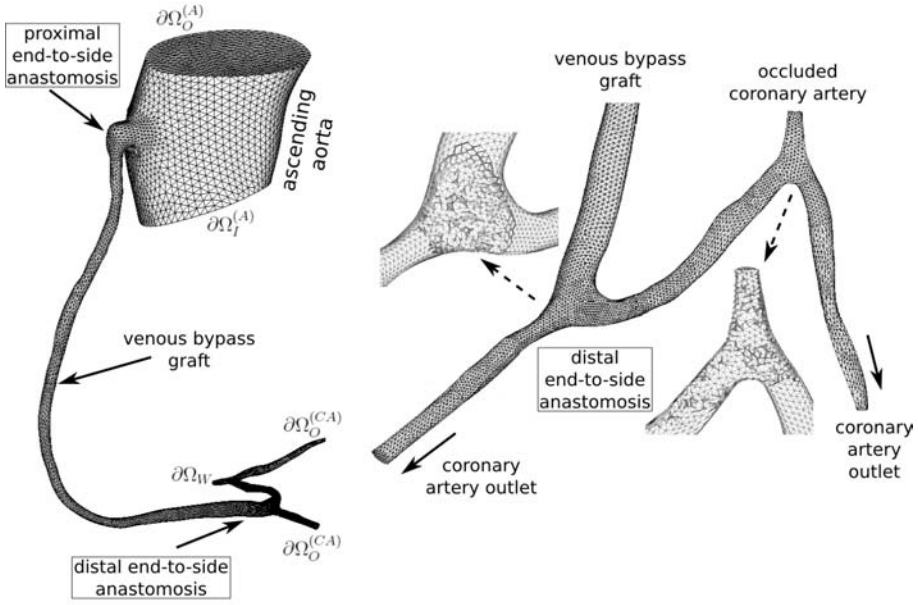

Fig. 3: Individual graft – unstructured computational mesh and relevant terminology

3. Mathematical model

Let us consider a time interval $(0, \mathcal{T})$, $\mathcal{T} > 0$ and a bounded three-dimensional computational domain $\Omega \subset \mathbf{R}^3$ with boundary $\partial\Omega = \partial\Omega_I \cup \partial\Omega_O \cup \partial\Omega_W$, where $\partial\Omega_I$, $\partial\Omega_O$ and $\partial\Omega_W$ denote the inlet, the outlet and the walls of the computational domain, respectively. In this study, coronary blood flow is modelled as unsteady laminar isothermal flow of incompressible generalised Newtonian fluid that in the space-time cylinder $\Omega_T = \Omega \times (0, \mathcal{T})$ is mathematically described by the non-linear system of incompressible Navier-Stokes (NS) equations written in the non-dimensional form

$$\frac{\partial v_i}{\partial x_i} = 0\,, \tag{2}$$

$$\frac{\partial v_i}{\partial t} + \frac{\partial}{\partial x_j}(v_i v_j) + \frac{\partial p}{\partial x_i} = \frac{1}{\mathrm{Re}}\frac{\partial}{\partial x_j}\left[\eta(\dot\gamma)\left(\frac{\partial v_i}{\partial x_j} + \frac{\partial v_j}{\partial x_i}\right)\right] \quad \text{for } i,j = 1,2,3\,, \tag{3}$$

where $t \in (0, \mathcal{T})$ is the time, v_i is the i-th component of the velocity vector $\boldsymbol{v} = [v_1, v_2, v_3]^T$ corresponding to the Cartesian component x_i of the space variables vector $\boldsymbol{x} = [x_1, x_2, x_3]^T \in \Omega$, p is the pressure, Re is the reference Reynolds number and $\eta(\dot\gamma)$ is the shear-dependent viscosity given by Eq. (1).

All variables appearing in Eqs. (2) – (3) are non-dimensionalized by the reference velocity $U_{ref} > 0$ and characteristic length $D_{ref} > 0$. For the bypass model considered in this study, the characteristic length value was chosen to be equal to the aorta diameter $D_{ref} \equiv D_{(A)} = 0.036\,\mathrm{m}$ and the reference velocity is stated as $U_{ref} = 4Q_0/(\pi\, D_{ref}^2) = 0.1592\,\mathrm{m}\cdot\mathrm{s}^{-1}$, where average aortic inlet flow rate is $Q_0 = 112.56 \cdot 10^{-6}\,\mathrm{m}^3\cdot\mathrm{s}^{-1}$, see Fig. 6 (left). As for the reference Reynolds number, it is determined as $\mathrm{Re} = U_{ref} D_{ref} \varrho/\eta_{ref} = 1\,744.3$, where $\varrho = 1050\,\mathrm{kg}\cdot\mathrm{m}^{-3}$ and $\eta_{ref} \equiv \eta_\infty = 3.45 \cdot 10^{-3}\,\mathrm{Pa}\cdot\mathrm{s}$. For the sake of completeness, reference pressure and reference time are computed as $p_{ref} = \varrho\, U_{ref}^2$ and $t_{ref} = D_{ref}/U_{ref}$, respectively.

4. Numerical method

The numerical solution of the non-linear time-dependent system of incompressible NS equations (2) – (3) is based on the projection method. In this study, the computation of velocity components v_i^{n+1}, which satisfy the divergence-free condition (2), employs the three-stage fractional step scheme, Ferziger and Perić (1999). In the first stage, intermediate velocity components v_i^* are explicitly computed from the convective part of the NS equation (3) as

$$\frac{v_i^* - v_i^n}{\Delta t} + \frac{\partial}{\partial x_j}(v_i^n v_j^n) = 0\,, \quad i,j = 1,2,3\,. \tag{4}$$

For the second stage of the fractional step scheme, the intermediate velocity components $\hat{v}_i$ are computed applying the unconditionally stable implicit Crank-Nicolson scheme to the viscous term of Eq. (3)

$$\frac{\hat{v}_i - v_i^*}{\Delta t} = \frac{1}{2\mathrm{Re}} \frac{\partial}{\partial x_j} \left[\eta(\dot{\gamma}) \left(\frac{\partial(\hat{v}_i + v_i^*)}{\partial x_j} + \frac{\partial(\hat{v}_j + v_j^*)}{\partial x_i} \right) \right], \quad i,j = 1,2,3. \tag{5}$$

Let us linearise the shear-dependent dynamic viscosity $\eta(\dot{\gamma})$ as $\overline{\eta}(\dot{\gamma}) = \eta(\dot{\gamma}(v^*))$ and introduce an auxiliary variable $d_{ij} = \frac{1}{2}\left(\frac{\partial v_i}{\partial x_j} + \frac{\partial v_j}{\partial x_i}\right)$, which in this case is equal to the components of the rate of deformation tensor **D** mentioned in section 2. Then Eq. (5) can be rewritten as a system of two linear equations

$$\frac{\hat{v}_i - v_i^*}{\Delta t} = \frac{1}{\mathrm{Re}} \frac{\partial}{\partial x_j} \left[\overline{\eta}(\dot{\gamma}) \left(\hat{d}_{ij} + d_{ij}^* \right) \right], \tag{6}$$

$$\hat{d}_{ij} = \frac{1}{2} \left(\frac{\partial \hat{v}_i}{\partial x_j} + \frac{\partial \hat{v}_j}{\partial x_i} \right). \tag{7}$$

In the third stage, pressure is used for the projection of the intermediate velocity vector $\hat{\boldsymbol{v}}$ onto a space of divergence-free velocity field to get the values of velocity and pressure at the next time level $(n+1)$. Hence, the velocity components v_i^{n+1} are computed from

$$\frac{v_i^{n+1} - \hat{v}_i}{\Delta t} + \frac{\partial p^{n+1}}{\partial x_i} = 0, \quad i = 1,2,3, \tag{8}$$

where p^{n+1} is computed from the Poisson equation for pressure

$$\frac{\partial^2 p^{n+1}}{\partial x_i \partial x_i} = \frac{1}{\Delta t} \frac{\partial \hat{v}_i}{\partial x_i}. \tag{9}$$

It can be easily shown that sum of Eqs. (4), (5) and (8) yields the approximation of NS equations of first order time accuracy. Finally, the whole algorithm of the fractional step method may be written for $i,j = 1,2,3$ as follows

$$v_i^* = v_i^n - \Delta t \frac{\partial}{\partial x_j} \left(v_i^n v_j^n \right), \tag{10}$$

$$\frac{\hat{v}_i}{\Delta t} - \frac{1}{\mathrm{Re}} \frac{\partial}{\partial x_j} \left(\overline{\eta}(\dot{\gamma})\, \hat{d}_{ij} \right) = \frac{v_i^*}{\Delta t} + \frac{1}{\mathrm{Re}} \frac{\partial}{\partial x_j} \left(\overline{\eta}(\dot{\gamma})\, d_{ij}^* \right), \tag{11}$$

$$\hat{d}_{ij} - \frac{1}{2} \left(\frac{\partial \hat{v}_i}{\partial x_j} + \frac{\partial \hat{v}_j}{\partial x_i} \right) = 0, \tag{12}$$

$$\frac{\partial^2 p^{n+1}}{\partial x_i \partial x_i} = \frac{1}{\Delta t} \frac{\partial \hat{v}_i}{\partial x_i}, \tag{13}$$

$$v_i^{n+1} = \hat{v}_i - \Delta t \frac{\partial p^{n+1}}{\partial x_i}. \tag{14}$$

The space discretization of the system of Eqs. (10) – (14) is performed using the cell-centred finite volume method for hybrid unstructured tetrahedral grids. The idea of applying the hybrid unstructured grid for the numerical solution of time-dependent incompressible NS equations in 2D was introduced in Kim and Choi (2000). The principle of this grid system lies in the coupling between an interpolation method, which will be described later, and the non-staggered grid system. Being inspired with this idea, we consider in this study a control volume Ω_k in the form of tetrahedron, Fig. 4. The hybrid grid system defines the values of pressure and Cartesian velocity components in the centre of the control volume Ω_k and the values of face-normal velocity V_m, which has the direction of outward unit vector $\boldsymbol{n}_k^m$ normal to the m-th face Γ_k^m of the control volume Ω_k, is defined in the middle of the face Γ_k^m.

After the integration of Eqs. (10) – (14) over each control volume Ω_k, Fig. 4, $k = 1,2,\ldots,N_{CV}$, where N_{CV} is the number of control volumes within the hybrid unstructured tetrahedral computational mesh, after the introduction of integral average for an arbitrary flow quantity Φ over the control volume Ω_k

$$(\Phi)_k = \frac{1}{|\Omega_k|} \int_{\Omega_k} \Phi \mathrm{d}\Omega, \tag{15}$$

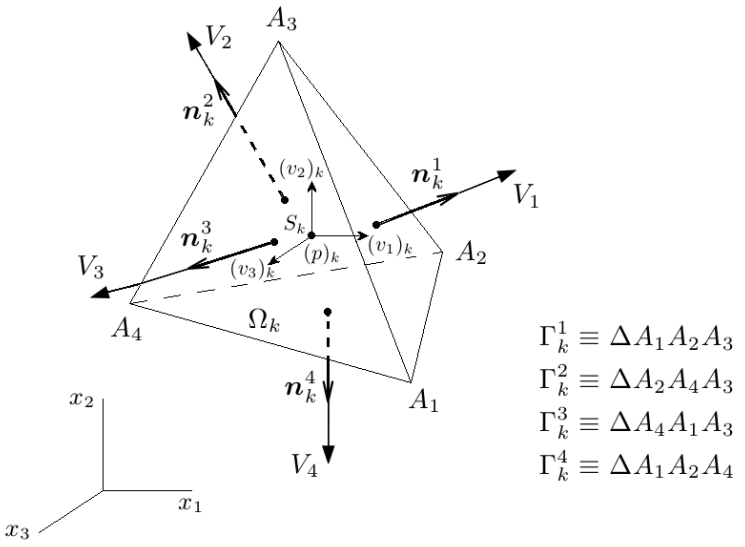

Fig. 4: A tetrahedral control volume $\Omega_k = A_1A_2A_3A_4$ with boundary $\partial\Omega_k = \bigcup_{m=1}^{4} \Gamma_k^m$ belonging to the hybrid unstructured computational mesh.

where $|\Omega_k|$ is the volume of the tetrahedral control volume Ω_k, and finally, after the application of the Gauss-Ostrogradsky theorem, which converts the volume integrals to surface integrals, we get

$$(v_i^*)_k = (v_i^n)_k - \frac{\Delta t}{|\Omega_k|} \oint\limits_{\partial\Omega_k} \left(v_j^n \cdot {}^j n_k\right) \cdot v_i^n \, \mathrm{d}\Gamma, \tag{16}$$

$$\frac{1}{\Delta t}(\hat{v}_i)_k - \frac{1}{\mathrm{Re}|\Omega_k|} \oint\limits_{\partial\Omega_k} \overline{\eta}(\dot{\gamma})\, \hat{d}_{ij} \cdot {}^j n_k \, \mathrm{d}\Gamma = \frac{1}{\Delta t}(v_i^*)_k + \frac{1}{\mathrm{Re}|\Omega_k|} \oint\limits_{\partial\Omega_k} \overline{\eta}(\dot{\gamma})\, d_{ij}^* \cdot {}^j n_k \, \mathrm{d}\Gamma, \tag{17}$$

$$\left(\hat{d}_{ij}\right)_k - \frac{1}{2}\left(\oint\limits_{\partial\Omega_k} \hat{v}_i \cdot {}^j n_k \, \mathrm{d}\Gamma + \oint\limits_{\partial\Omega_k} \hat{v}_j \cdot {}^i n_k \, \mathrm{d}\Gamma \right) = 0\,, \tag{18}$$

$$\oint\limits_{\partial\Omega_k} \frac{\partial p^{n+1}}{\partial \boldsymbol{n}_k} \, \mathrm{d}\Gamma = \frac{1}{\Delta t} \oint\limits_{\partial\Omega_k} \hat{v}_i \cdot {}^i n_k \, \mathrm{d}\Gamma, \tag{19}$$

$$(v_i^{n+1})_k = (\hat{v}_i)_k - \frac{\Delta t}{|\Omega_k|} \oint\limits_{\partial\Omega_k} p^{n+1} \cdot {}^i n_k \, \mathrm{d}\Gamma, \tag{20}$$

where ${}^i n_k$ is the i-th component of the outward unit vector $\boldsymbol{n}_k = [{}^1 n_k, {}^2 n_k, {}^3 n_k]^T$ normal to the boundary $\partial\Omega_k$ of the tetrahedral control volume Ω_k, Fig. 4. In order to achieve the satisfaction of the continuity equation for the normal velocity $V = v_i \cdot {}^i n_k$, the system of Eqs. (16) – (20) is completed with following equation

$$V^{n+1} = \hat{V} - \Delta t \, \frac{\partial p^{n+1}}{\partial \boldsymbol{n}_k}\,. \tag{21}$$

This equation defines the normal velocity V^{n+1} at the time level $(n+1)$ having the direction of the outward unit vector $\boldsymbol{n}_k$ normal to the boundary $\partial\Omega_k$ of the control volume Ω_k. For the intermediate normal velocity $\hat{V}$, it is valid that $\hat{V} = \hat{v}_i \cdot {}^i n_k$.

Further, we perform the approximation of surface integrals in the system of Eqs. (16) – (20). Firstly, each integral is replaced by the sum of integrals over each face Γ_k^m of the control volume Ω_k, Fig. 4, and

then approximated by the midpoint rule

$$\oint_{\partial\Omega_k} \Phi \, \mathrm{d}\Gamma = \sum_{m=1}^{4} \int_{\Gamma_k^m} \Phi \, \mathrm{d}\Gamma \approx \sum_{m=1}^{4} \Phi_m |\Gamma_k^m|, \tag{22}$$

where $|\Gamma_k^m|$, $m = 1, \ldots, 4$ is the area of the m-th face Γ_k^m of the control volume Ω_k and Φ_m is the value of an arbitrary flow quantity at the integration point at the same face. The interpolation process needed for the determination of Φ_m at the m-th face Γ_k^m of the control volume Ω_k will be described later. Using Eq. (22), the system of Eqs. (16) – (21) is modified as follows

$$(v_i^*)_k = (v_i^n)_k - \frac{\Delta t}{|\Omega_k|} \sum_{m=1}^{4} \left(V_m^n \cdot v_{i\,m}^n|_{\text{upwind}} \right) |\Gamma_k^m| \,, \tag{23}$$

$$\frac{(\hat{v}_i)_k}{\Delta t} - \frac{1}{\mathrm{Re}\,|\Omega_k|} \sum_{m=1}^{4} \overline{\eta}(\dot{\gamma})^m \, \hat{d}_{ij}^m \cdot {}^j n_k^m \, |\Gamma_k^m| = \frac{(v_i^*)_k}{\Delta t} + \frac{1}{\mathrm{Re}\,|\Omega_k|} \sum_{m=1}^{4} \overline{\eta}(\dot{\gamma})^m \, d_{ij}^{*m} \cdot {}^j n_k^m \, |\Gamma_k^m|, \tag{24}$$

$$\left(\hat{d}_{ij}\right)_k - \frac{1}{2} \left(\sum_{m=1}^{4} \hat{v}_{i\,m} \cdot {}^j n_k^m |\, \Gamma_k^m| \; + \; \sum_{m=1}^{4} \hat{v}_{j\,m} \cdot {}^i n_k^m |\, \Gamma_k^m| \right) = 0 \,, \tag{25}$$

$$\sum_{m=1}^{4} \frac{\partial p^{n+1}}{\partial \boldsymbol{n}_k^m} |\Gamma_k^m| = \frac{1}{\Delta t} \sum_{m=1}^{4} \hat{v}_{i\,m} \cdot {}^i n_k^m |\, \Gamma_k^m| \equiv \frac{1}{\Delta t} \sum_{m=1}^{4} \hat{V}_m \, |\Gamma_k^m|, \tag{26}$$

$$(v_i^{n+1})_k = (\hat{v}_i)_k - \frac{\Delta t}{|\Omega_k|} \sum_{m=1}^{4} p_m^{n+1} \cdot {}^i n_k^m \, |\Gamma_k^m| \,, \tag{27}$$

$$V_m^{n+1} = \hat{V}_m - \Delta t \, \frac{\partial p^{n+1}}{\partial \boldsymbol{n}_k^m} \,, \tag{28}$$

where ${}^i n_k^m$ is the i-th component of the outward unit vector $\boldsymbol{n}_k^m = [{}^1 n_k^m, \, {}^2 n_k^m, \, {}^3 n_k^m]^T$ normal to the m-th face Γ_k^m of the control volume Ω_k and for the intermediate face-normal velocity $\hat{V}_m$ at the m-th face Γ_k^m of the control volume Ω_k, it is valid that $\hat{V}_m = \hat{v}_{im} \cdot {}^i n_k^m$. Note that the values of face-normal velocity V_m^{n+1} computed with the help of Eq. (28) are used as values of face-normal velocity V_m^n in Eq. (23) at the next time level.

Explicit schemes are known for their disadvantage in the form of restricted time steps. The CFL stability condition imposed on the time step size becomes essential when it is applied for grids with large differences in cell size, e.g., in complex geometries. In this case, the efficiency of explicit schemes is lost, since the cell with the most restrictive local time step determines the size of the global time step for all grid cells. One of possible solutions to this problem lies in the application of the well-known local time-stepping method. This method, whose approach is also employed in our developed solver, enables each cell of the computational grid to run with its own time step in a time-consistent manner.

Interpolation method

To perform numerical computations according to Eqs. (23) – (28), it is necessary to determine values of $v_{i\,m}^n|_{\text{upwind}}$, $\hat{v}_{i\,m}$, p_m^{n+1} and derivatives $\frac{\partial \hat{v}_i}{\partial \boldsymbol{n}_k^m}$, $\frac{\partial v_i^*}{\partial \boldsymbol{n}_k^m}$, $\frac{\partial p^{n+1}}{\partial \boldsymbol{n}_k^m}$ at the m-th face Γ_k^m of the control volume Ω_k. The value of $v_{i\,m}^n|_{\text{upwind}}$ is computed by the upwind scheme, whose first order accuracy is increased by linear reconstruction with Barth's limiter,

$$v_{i\,m}^n|_{\text{upwind}} = \begin{cases} (v_i^n)_L + \sigma_L^{Barth} \cdot \frac{\partial (v_i^n)_L}{\partial x_j} \cdot r_{jL} \,, & V_m^n > 0 \,, \\ (v_i^n)_R + \sigma_R^{Barth} \cdot \frac{\partial (v_i^n)_R}{\partial x_j} \cdot r_{jR} \,, & V_m^n \leq 0 \,, \end{cases} \tag{29}$$

where $\sigma^{Barth} \in [0, 1]$ is the Barth's limiter, Barth and Jesperson (1989), and vectors $\boldsymbol{r}_L$, $\boldsymbol{r}_R$ are denoted in Fig. 5 (*left*). Further, the value Φ_m of an arbitrary flow quantity Φ at the mid-point O of the m-th face Γ_k^m, Fig. 5 (*right*), can be stated with the help of second order accurate linear interpolation from

values $(\Phi)_k$ and $(\Phi)_{l_m}$ defined in cell-centres S_k and S_{l_m} of two adjacent control volumes Ω_k and Ω_{l_m}, respectively,

$$\Phi_m = (\Phi)_k + \frac{(\Phi)_{l_m} - (\Phi)_k}{\gamma_k + \gamma_{l_m}} \cdot \gamma_k = \frac{\gamma_{l_m}(\Phi)_k + \gamma_k(\Phi)_{l_m}}{\gamma_k + \gamma_{l_m}}\,, \tag{30}$$

where γ_k and γ_{l_m} are the minimal distances to the cell-face Γ_k^m from cell-centres S_k and S_{l_m} of the adjacent control volumes Ω_k and Ω_{l_m}, respectively, Fig. 5 (*right*). The derivative of flow quantity Φ in the direction of the outward unit vector $\boldsymbol{n}_k^m$ normal to the m-th face Γ_k^m of the control volume Ω_k, is approximated at the mid-point O of the face Γ_k^m, Fig. 5 (*right*), as

$$\left.\frac{\partial \Phi}{\partial \boldsymbol{n}_k^m}\right|_{\Gamma_k^m} \approx \frac{(\Phi)_{l_m} - (\Phi)_k}{\gamma_k + \gamma_{l_m}}. \tag{31}$$

A crucial part of the interpolation method is the application of Eq. (31) to the normal derivative in Eqs. (26) and (28). In this way, it is ensured that the face-normal velocity V_m^{n+1} satisfies the continuity equation at the time level $(n+1)$ exactly, see Eq. (37). However, in general velocities $(v_i^{n+1})_k$ in cell-centres of control volumes Ω_k do not satisfy the continuity equation.

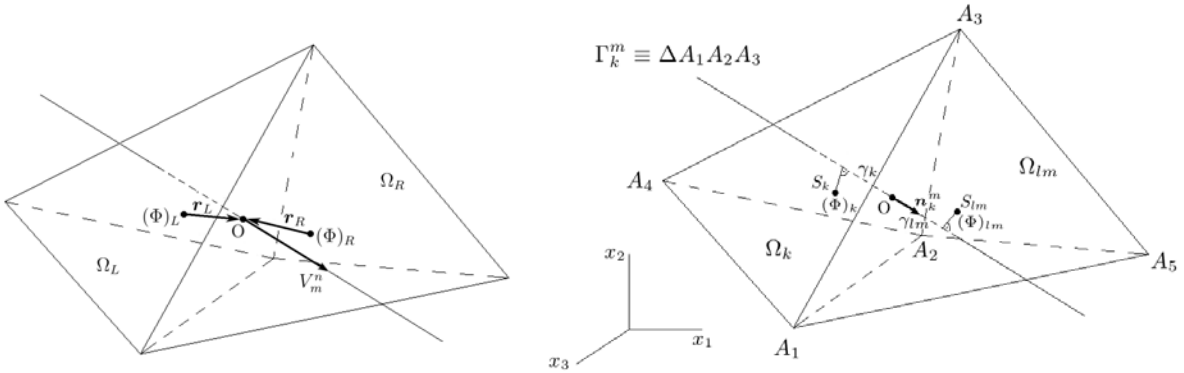

Fig. 5: Definition of the vectors $\boldsymbol{r}_L$ and $\boldsymbol{r}_R$ for two adjacent tetrahedral control volumes Ω_L and Ω_R (left). Two adjacent tetrahedral control volumes $\Omega_k = A_1A_2A_3A_4$ and $\Omega_{l_m} = A_1A_2A_3A_5$ with their contact face $\Gamma_k^m = \Delta A_1A_2A_3$ (right).

Regarding the implementation of non-dimensional *boundary conditions* at the boundary $\partial\Omega$ of the computational domain $\Omega \subset \mathbf{R}^3$, three boundary types are considered in this study:

- **inlet** $\Gamma_k^m \subset \partial\Omega_I$ – In this case, Dirichlet boundary conditions for the velocity components $v_{i\,m}$ and the auxiliary variable d_{ij}^m are prescribed

$$v_{i\,m} = v_{i\,I}\,, \qquad d_{ij}^m \cdot {}^j n = 0. \tag{32}$$

  The value of face-normal velocity V_m^I at the face Γ_k^m is computed as $V_m^I = v_{i\,I} \cdot {}^i n_k^m$, where values $v_{i\,I}$ are given according to section 5. For the normal derivative of the pressure p^{n+1} at the face Γ_k^m, we prescribe

$$\left.\frac{\partial p^{n+1}}{\partial \boldsymbol{n}_k^m}\right|_{\Gamma_k^m} = 0. \tag{33}$$

- **rigid and impermeable wall** $\Gamma_k^m \subset \partial\Omega_W$ – Velocity components $v_{i\,m}$ at the face Γ_k^m are set equal to zero

$$v_{i\,m} = 0\,, \tag{34}$$

  leading to zero value of the face-normal velocity $V_m^W = v_{i\,m} \cdot {}^i n_k^m = 0$ at the face Γ_k^m. For the auxiliary variable d_{ij}^m, we apply the Dirichlet boundary condition in the following form

$$d_{ij}^m \cdot {}^j n = 0\,. \tag{35}$$

  Further, zero normal derivative of the pressure p^{n+1} (33) is prescribed at the wall.

- **outlet** $\Gamma_k^m \subset \partial\Omega_O$ – Following type of boundary condition is stated

$$p_m \boldsymbol{n}_k^m - \frac{1}{\mathrm{Re}} 2\,\overline{\eta}(\dot{\gamma})^m\, d_{ij}^m \cdot {}^j n_k^m = p_O \boldsymbol{n}_k^m, \tag{36}$$

  where p_O is the given value of the outlet pressure, for details see section 5.

Substituting the derivative $\frac{\partial p^{n+1}}{\partial \boldsymbol{n}_k^m}$ in Eq. (26) with Eq. (28), we get

$$\begin{aligned} \sum_{m=1}^{4} \frac{\partial p^{n+1}}{\partial \boldsymbol{n}_k^m} |\Gamma_k^m| \;\; &= \frac{1}{\Delta t} \sum_{m=1}^{4} \left(\hat{V}_m - V_m^{n+1} \right) |\Gamma_k^m| = \frac{1}{\Delta t} \sum_{m=1}^{4} \hat{V}_m\, |\Gamma_k^m| \\ &\Longrightarrow \sum_{m=1}^{4} V_m^{n+1} |\Gamma_k^m| = 0, \end{aligned} \tag{37}$$

i.e., face-normal velocities V_m^{n+1} satisfy the continuity equation exactly. At this point, let us mention that at the outlet boundary $\partial\Omega_O$, i.e., at the face Γ_k^m of the control volume Ω_k, where $\Gamma_k^m \subset \partial\Omega_O$, values $\frac{\partial p^{n+1}}{\partial \boldsymbol{n}_k^m}$ are unknown. In order to ensure the satisfaction of the continuity equation (37) for this control volume Ω_k, it is necessary to compute the face-normal velocity V_m^{n+1} at the face $\Gamma_k^m \subset \partial\Omega_O$ as

$$V_{m_O}^{n+1} = -\frac{1}{|\Gamma_k^{m_O}|} \sum_{\substack{m=1 \\ m \neq m_O}}^{4} V_m^{n+1} |\Gamma_k^m|, \tag{38}$$

where m_O is the index of the outlet face $\Gamma_k^{m_O}$ of the control volume Ω_k. For the whole computational domain $\Omega \subset \mathbf{R}^3$ at the time $t = 0$, following *initial conditions* are used

$$(v_i^0)_k = \frac{1}{|\Omega_k|} \int_{\Omega_k} v_i(\boldsymbol{x}, 0) \mathrm{d}\Omega = 0, \qquad (p^0)_k = \frac{1}{|\Omega_k|} \int_{\Omega_k} p(\boldsymbol{x}, 0) \mathrm{d}\Omega = p_{initial},\ k = 1, 2, \ldots, N_{CV},$$

where $p_{initial}$ is a non-dimensional value of static pressure.

5. Numerical results

In accordance with the boundaries of the computational domain denoted in Fig. 3 for the model of the individual aorto-coronary bypass, the numerical simulations of pulsatile Newtonian and non-Newtonian blood flow are carried out with following values of the time-dependent boundary conditions:

- aortic inlet $\partial\Omega_I^{(A)}$ – constant time-dependent velocity profile $|\boldsymbol{v}_I|$ according to the flow rate waveform $Q(t)$ shown in Fig. 6 (left);
- aortic outlet $\partial\Omega_O^{(A)}$ – time-dependent pressure $p(t)$ shown in Fig. 6 (right), where the aortic pressure is plotted in the medical units of millimeters of mercury (1 mmHg $= 133.333$ Pa);
- coronary outlets $\partial\Omega_O^{(CA)}$ – constant pressure related to average arterial pressure of 12 000 Pa;
- rigid and impermeable walls $\partial\Omega_W$ – non-slip boundary condition.

Note that the boundary values mentioned above are, for the computation, non-dimensionalized using the reference values mentioned in section 3. The implementation of the boundary conditions in the numerical code is described in detail in section 4.

For the analysis of computed numerical results, we introduce two significant hemodynamical wall parameters – the cycle-averaged wall shear stress (WSS) and the oscillatory shear index (OSI) that are evaluated according to formulas mentioned in Xiong and Chong (2008) and He and Ku (1996), respectively,

$$\overline{|\boldsymbol{\tau}_W|} = \frac{1}{T} \int_0^T |\boldsymbol{\tau}_W| \mathrm{d}t\,, \qquad \mathrm{OSI} = \frac{1}{2} \left[1 - \left| \int_0^T \boldsymbol{\tau}_W \mathrm{d}t \right| \cdot \left(\int_0^T |\boldsymbol{\tau}_W| \mathrm{d}t \right)^{-1} \right], \tag{39}$$

where $|\boldsymbol{\tau}_W|$ is the WSS magnitude and $T = 1$ s is the duration of one cardiac cycle, Fig. 6.

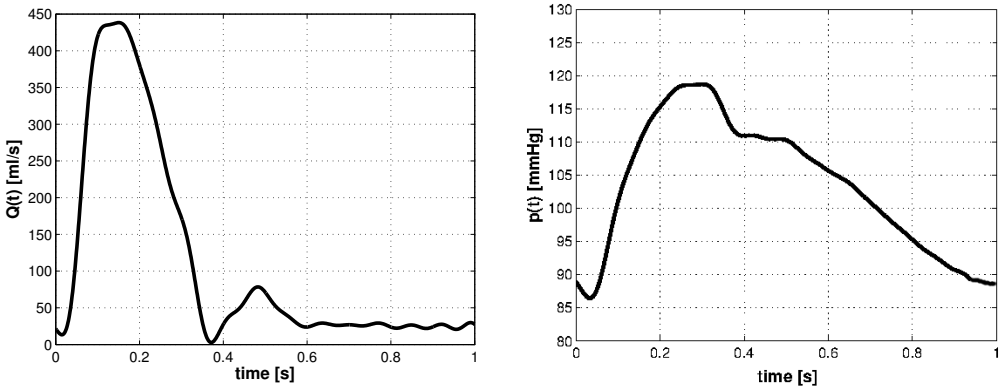

Fig. 6: Time-dependent boundary conditions for the aorta – inlet flow rate $Q(t)$ (left) and outlet pressure $p(t)$ (right), data taken from Olufsen et al. (2000)

Firstly, let us analyse the velocity profiles of the non-Newtonian blood flow in Fig. 7 for three selected time instants, corresponding to systole, diastole and late diastole, respectively. During the systolic phase ($t_1 = 0.16\,\mathrm{s}$), Fig. 7 (left), the graft's proximal anastomosis becomes exposed to the increased flow rate in the aorta. Although the skewed velocity profiles at the graft entrance may indicate incoming blood flow, the real graft filling occurs later. By comparing the pictures in Fig. 7, it becomes quite apparent that the systolic phase of the cardiac cycle is represented by decreased blood flow through the individual bypass graft, whereas an opposite effect is observed during most of the diastolic phase ($t_2 = 0.47\,\mathrm{s}$ and $t_3 = 0.98\,\mathrm{s}$). In this case, the velocity increase observed along the individual graft is also accompanied by skewed or otherwise shaped velocity profiles that are a result of the out-of-plane geometry and the graft's winding around the heart, see Fig. 2. At the distal end-to-side anastomosis, Fig. 7c, the incoming blood flow seems to prefer the closer branch of the coronary artery more than the second one. Moreover, the closer coronary artery shows a tendency to considerably increase velocity magnitude downstream from the anastomosis. The reason for this phenomenon is a partly stenosed coronary artery.

The comparison between the Newtonian and non-Newtonian blood flow is illustrated by the distributions of the cycle-averaged WSS and OSI in Figs. 8 and 9, respectively. At this point, note the lowered value range in Fig. 8, which is chosen according to conclusions mentioned in Haruguchi and Teraoka (2003) and He and Ku (1996). Namely, that low WSS, as compared to the normal range between $1 - 2\,\mathrm{Pa}$ in healthy arteries, is one of the confirmed triggers of vessel remodelling, plaque growth and intimal thickening. In light of this fact, we will further assess the resulting shear distribution, which regardless of the viscosity model (Newtonian or non-Newtonian), seems to be non-uniform at both anastomoses, Fig. 8. One of the distinct areas with extremely low shear is situated at the entrance of the graft, where it is caused by a large recirculation zone that is present there most of the cardiac cycle. This negative stimulation of the proximal suture line is also confirmed by the high OSI shown in Fig. 9. At the distal anastomosis, shear values below $1\,\mathrm{Pa}$ are observed at the heel and the arterial floor in accordance with the sites of intimal hyperplasia displayed in Fig. 1. In this case, the critical shear stress also shows a oscillatory tendency as is apparent from the OSI distribution in Fig. 9.

The objective of our previous study, Vimmr and Jonášová (2010), was the investigation of blood's non-Newtonian behaviour in complete bypass models with coronary or femoral native arteries. The numerical simulations were carried out under steady flow conditions and for an idealized bypass geometry. In the present study, we want to extend our previous conclusions about the importance of blood's non-Newtonian modelling in coronary bypasses by considering pulsatile blood flow and a realistic and more complex bypass geometry. As is illustrated by Figs. 8 – 9, the influence of non-Newtonian flow conditions is very small or rather negligible (as is the case of the velocity profiles). On the basis of these observations, we can draw a conclusion similar to that mentioned in Vimmr and Jonášová (2010). Namely, that blood's non-Newtonian behaviour does not have any significant impact on the hemodynamics in coronary bypasses. In light of this observation and our present experience with the modelling of non-Newtonian blood flow, it may be said that an hemodynamic study in patient-specific femoral bypasses would be more promising in regard to the occurrence of non-Newtonian effects as was concluded in our previous study Vimmr and Jonášová (2010). This problem will be addressed in the future.

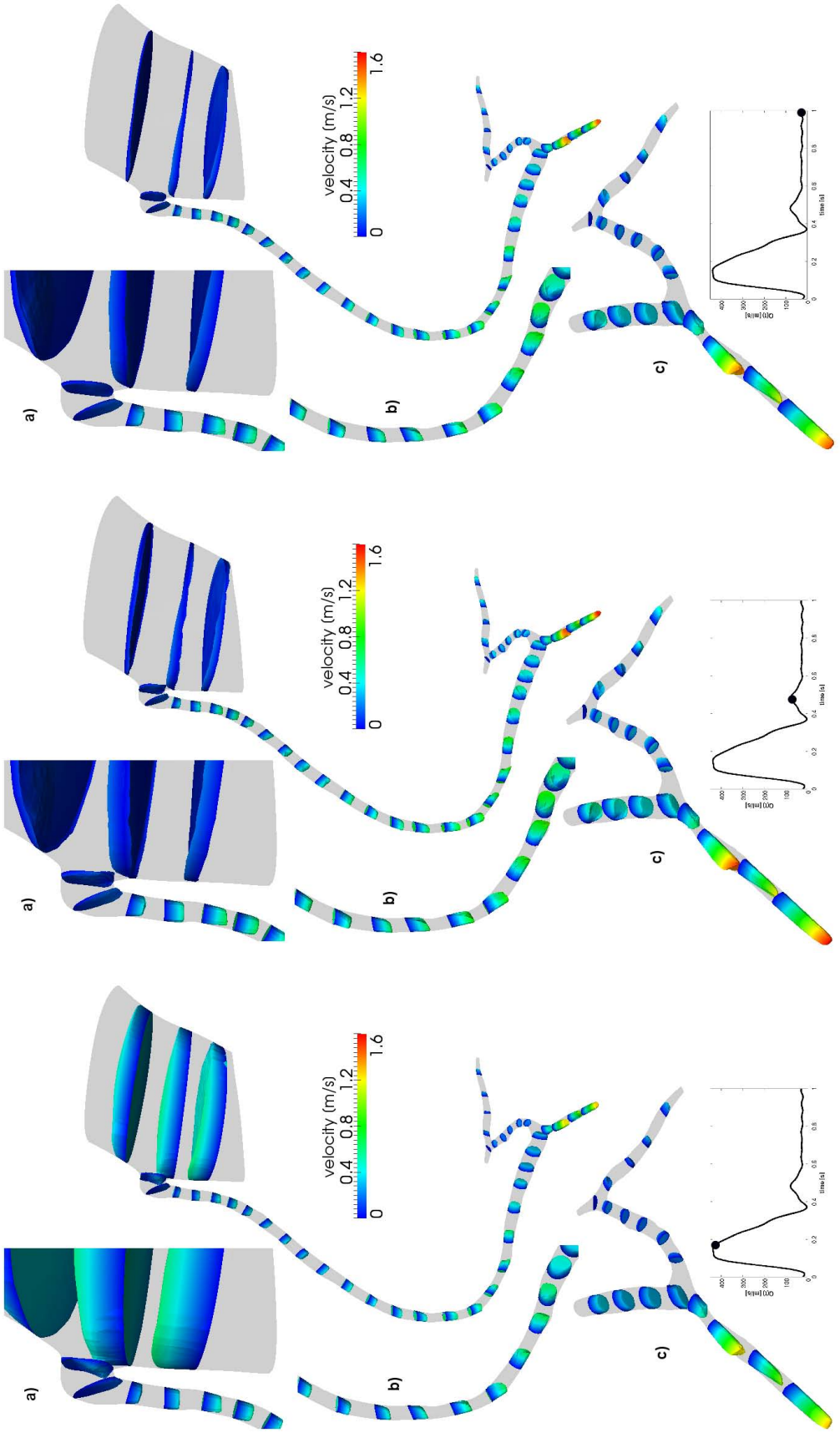

Fig. 7: Non-Newtonian blood flow – velocity profiles at selected cross-sections of the aorto-coronary bypass at the time instants $t_1 = 0.16\,s$, $t_2 = 0.47\,s$ and $t_3 = 0.98\,s$ (from left to right); detailed views at (a) the proximal anastomosis, (b) individual graft, (c) coronary arteries with the distal anastomosis

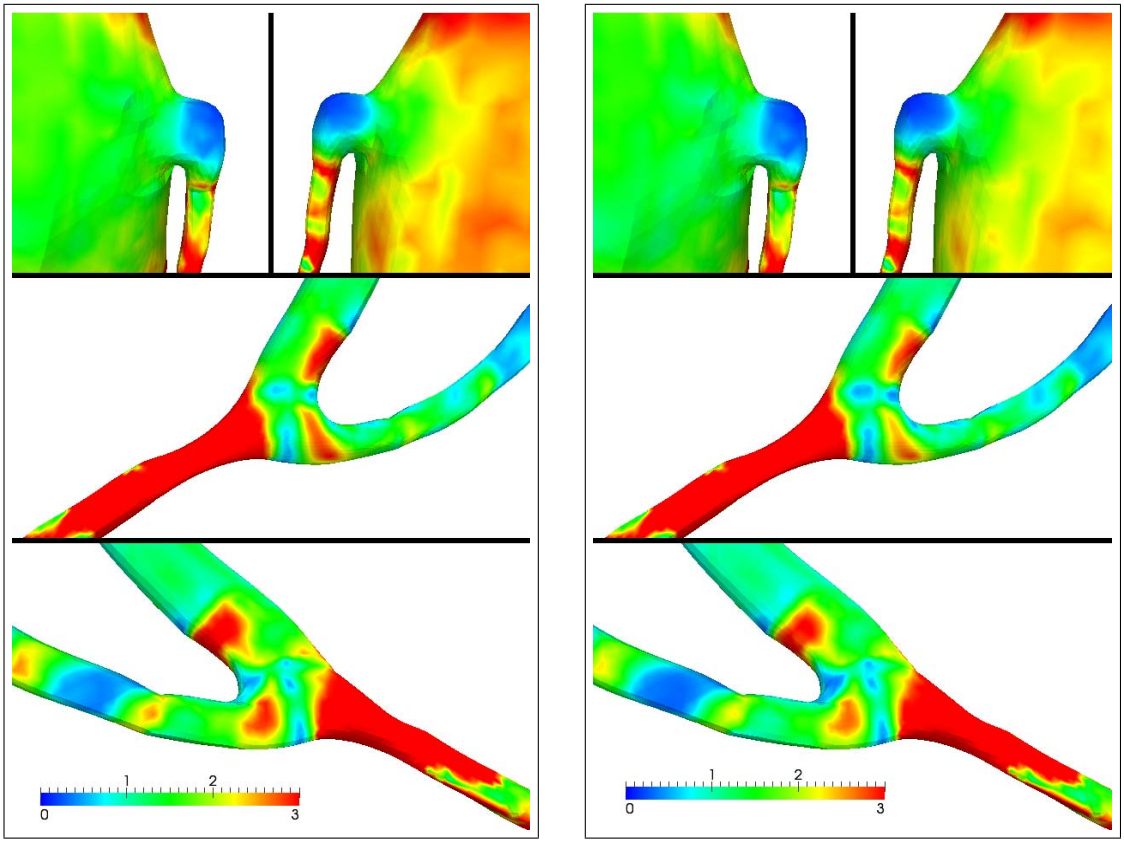

Fig. 8: Distribution of cycle-averaged WSS for the Newtonian (left) and non-Newtonian flow (right)

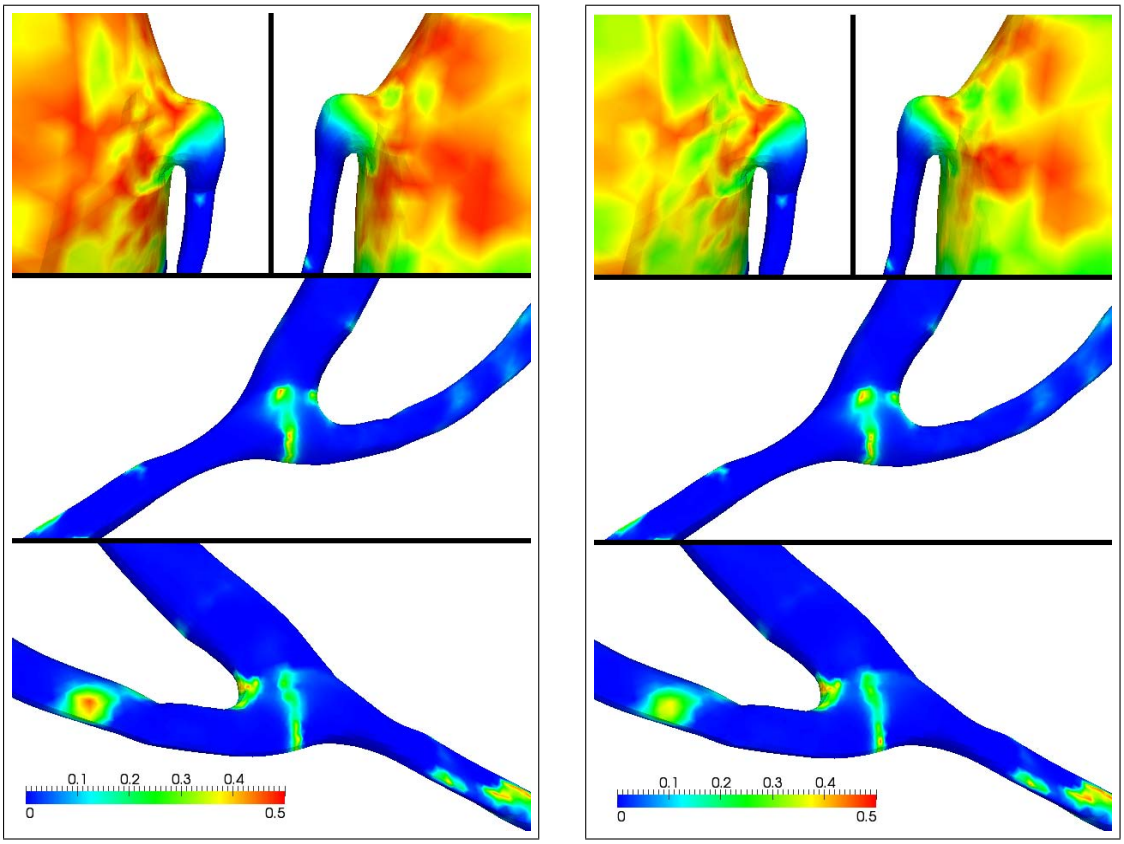

Fig. 9: Distribution of OSI for the Newtonian (left) and non-Newtonian flow (right)

Acknowledgments

This study was supported by the European Regional Development Fund (ERDF), project NTIS - New Technologies for Information Society, European Centre of Excellence, CZ.1.05/1.1.00/02.0090 and by the internal student grant project SGS-2010-046 of the University of West Bohemia.

References

Bassiouny, H.S., White, S., Glagov, S., Choi, E., Giddens, D.P., Zarins, C.K. (1992), Anastomotic intimal hyperplasia: Mechanical injury or flow induced. *Journal of Vascular Surgery*, Vol 15, No.4, pp 708-717.

Barth, T.J., Jesperson, D.C. (1989), The design and application of upwind schemes on unstructured meshes. In: *Proceedings of the 27th AIAA Aerospace Sciences Meeting*. AIAA Paper 89-0366.

Cho, Y.I., Kensey, K.R. (1991), Effects of the non-Newtonian viscosity of blood on flows in diseased arterial vessels. Part I: Steady flows. *Biorheology*, Vol 28, No.3-4, pp 241-262.

Ferziger, J.H., Perić M. (1999), *Computational methods for fluid dynamics*, Springer, Heidelberg.

Haruguchi, H., Teraoka, S. (2003), Intimal hyperplasia and hemodynamic factors in arterial bypass and arteriovenous grafts: A review. *Journal of Artificial Organs*, Vol 6, No.4, pp 227-235.

He, X., Ku, D.N. (1996), Pulsatile flow in the human left coronary artery bifurcation: Average conditions. *Journal of Biomechanical Engineering*, Vol 118, No.1, pp 74-82.

Kim, D., Choi, H. (2000) A second-order time accurate finite volume method for unsteady incompressible flow on hybrid unstructured grids. *Journal of Computational Physics*, Vol 162, No.2, pp 411-428.

Loth, F., Fischer, P.F., Bassiouny, H.S. (2008) Blood flow in end-to-side anastomoses. *Annual Review of Fluid Mechanics*, Vol 40, pp 367-393.

Olufsen, M.S., Peskin, C.S., Kim, W.Y., Pedersen, E.M., Nadim, A., Larsen, J. (2000) Numerical simulation and experimental validation of blood flow in arteries with structured-tree outflow conditions. *Annals of Biomedical Engineering*, Vol 28, No.11, pp 1281-1299.

Vimmr, J., Jonášová, A. (2010), Non-Newtonian effects of blood flow in complete coronary and femoral bypasses. *Mathematics and Computers in Simulation*, Vol 80, No.6, pp 1324-1336.

Vural, K.M., Şener, E., Taşdemir, O. (2001) Long-term patency of sequential and individual saphenous vein coronary bypass grafts. *European Journal of Cardio-thoracic Surgery*, Vol 19, No.2, pp 140-144.

Xiong, F.L., Chong, C.K. (2008), A parametric numerical investigation on haemodynamics in distal coronary anastomoses. *Medical Engineering & Physics*, Vol 30, No.3, pp 311-320.

Zeng, D., Ding, Z., Friedman, M.H., Ethier, C.R. (2003), Effects of cardiac motion on right coronary artery hemodynamics. *Annals of Biomedical Engineering*, Vol 31, No.4, pp 420-429.